Electronic Supplementary Material (ESI) for Nanoscale.
This journal is © The Royal Society of Chemistry 2017

Supporting information for:

Lifetimes Nanomanometry - High-Pressure Luminescence of Up-converting Lanthanide Nanocrystals - $SrF_2:Yb^{3+}, Er^{3+}$

Marcin Runowski,[1] Jędrzej Marciniak,[1] Tomasz Grzyb,[1] Dominika Przybylska,[1] Andrii Shyichuk,[2] Bolesław Barszcz,[3] Andrzej Katrusiak[1*] and Stefan Lis[1*]

[1]*Adam Mickiewicz University, Faculty of Chemistry, Umultowska 89b, 61-614 Poznań, Poland*

[2]*Faculty of Chemistry, University of Wrocław, F. Joliot-Curie 14, 50-383 Wrocław, Poland*

[3]*Institute of Molecular Physics, Polish Academy of Sciences, Mariana Smoluchowskiego 17, 60-179 Poznań, Poland*

Experimental

Materials

Rare earth (RE) oxides: Er_2O_3 and Yb_2O_3 (99.99%, Stanford Materials, United States) were dissolved separately in hydrochloric acid, HCl (ultra-pure, Sigma-Aldrich, 37%, Poland) in order to obtain respective rare earth chloride solutions in a concentration of 1 or 0.25M. Ammonium fluoride, NH_4F (98+%, Sigma-Aldrich, Poland) was used as the source of fluoride ions. Strontium chloride hexahydrate $SrCl_2{\cdot}6H_2O$ (Sigma-Aldrich, 99+%, Poland) and citric acid trisodium salt dihydrate, (Sigma-Aldrich, 97 %, Poland) were used as received, without further purification. Deionized water was used for the synthesis.

Synthesis of SrF_2: 20% Yb^{3+}, 1% Er^{3+} nanoparticles

In order to obtain 3.5 mmol of SrF_2 doped with 20 mol.% of Yb^{3+} and 1 mol.% of Er^{3+}, the aqueous solutions of $SrCl_2$ (2.77 mmol; 2.77 mL, 1 M) and $LnCl_3$ (0.8 mmol; 0.70 mL of 1 M $YbCl_3$ and 0.14 mL of 0.25 M $ErCl_3$) were added to 20 mL of 1 M aqueous solution of sodium citrate (anti-agglomeration and complexing agent). Then, 5 mL of 4.2 M aqueous solution of NH_4F (a source of fluoride ions) was added to the solution containing $SrCl_2$ and $LnCl_3$ salts. The pH of the final solution was equal to 7.5. The as-prepared transparent solution was transferred into Teflon-lined vessel and hydrothermally treated for 12 h (180^{o}C, 10 bar), in an externally heated autoclave. When the reaction was completed, the obtained white precipitate was purified by centrifugation and rinsed several times with water and ethanol. The final product was dried at ambient conditions. The exact elemental composition of the synthesized NPs, determined by ICP-OES analysis is 1.1 mol.% Er, 21.9 mol.% Yb and 77 mol.% Sr.

DAC loading procedure

High-pressure X-ray diffraction experiments were performed in a Merrill-Bassett diamond-anvil cell (DAC),[1] modified by mounting the anvils directly on steel supporting plates.[2] The gaskets were made of stainless steel foil 0.25 mm thick with the aperture of 0.5 mm. Pressure was determined from the ruby R1 fluorescence line shifts[3] by using a Photon Control spectrometer affording an accuracy of 0.03 GPa. The DAC chamber was filled with SrF2:Yb,Er nanocrystals and methanol:etahanol (4:1 vol.) mixture to ensure hydrostaticity.

Pressure calibration

Before each measurement the value of the pressure in the DAC was determined on the basis of the spectral shift of ruby fluorescence (R1 ruby line), as its emission bands exhibit red-shift with increasing pressure. The source of excitation was continuous wave, 532 nm, diode-pumped solid-state laser (8 mW). The measurements were performed at ambient conditions, using a standard ruby calibration curve.[4]

Structural measurements - XRD

Single-crystal diffractometer Xcalibur EOS CCD with Mo Kα X-ray source was used for diffraction measurements; the powder data were collected at 0.0001, 0.03, 0.15, 0.25, 0.50, 0.77, 1.05, 1.24, 1.52, 1.99, 2.55, 3.24, 3.50, 3.99, 4.52, 5.02 and 5.29 GPa upon compression, and at 3.77, 2.08, 1.00 and 0.0001 GPa upon decompression. The CrysAlisPro program suite was used for initial analysis of the diffraction data.[5]

Luminescence measurements

The measurements of high-pressure, up-conversion emission of the sample placed in the DAC were performed in an optimized configuration, using an unconventional ≈ 45 degree detection geometry (the NIR excitation light was in a 45 degree angle with the detector). We have found experimentally that such a configuration for the luminescence measurements in a DAC provided much more intense luminescence signal, in comparison with the commonly used 180 degree detection geometry (transmitting mode). It is worth noting, that a conventional fluorescence measurements using the 90 degree detection geometry could not be applied due to the opening angle of the DAC window (in our case 60 degree). The setup for our luminescence measurements is schematically shown in Figure 1 in the main manuscript. Each luminescence measurement was repeated 3-times and averaged, resulting in uncertainties presented as error bars. The approximated laser power density values used for the experiments were ≈100 W/cm^2 for continuous laser and ≈100 mJ/cm^2 for pulsed one.

Characterization

Transmission electron microscopy (TEM) measurements were performed using a FEI Tecnai G2 20 X-TWIN microscope, operating at 200 kV. Powder XRD patterns were recorded with a single-crystal Xcalibur EOS CCD diffractometer using Mo Kα radiation (λ = 0.710806 Å). The emission spectra and the determined integral luminescence intensities were measured using a continuous 980 nm diode-pumped solid-state laser (Dragonlasers, 2 W). Whereas, luminescence decay curves and excitation spectra were recorded using the tunable Opolette 355LD UVDM pulsed laser with repetition rate of 20 Hz (Opotek Inc.) as excitation source and QuantaMaster^{TM} 40 spectrophotometer (Photon Technology International) with R928 photomultiplier as a detector (from Hamamatsu). All spectra were measured at 293 K and were appropriately corrected for the instrumental response. The Raman spectra were recorded in backscattering geometry using an Ar+ laser (Stabilite 2017, Spectra Physics) operating at 514.53 nm and about 12 mW at the sample. The laser beam was focused using a x20 LWD (Long Working Distance) objective. The scattered light was analyzed by a LabRAM HR800 (HORIBA Jobin Yvon) spectrometer equipped with liquid nitrogen cooled CCD detector. For calibration of the Raman Shift the Si line at 520.7 cm-1 was used. The exposition time for single spectrum accumulation was 3 s and the resulting spectrum was determined after averaging 10 accumulations. All Raman measurements were made at room temperature (295 K).

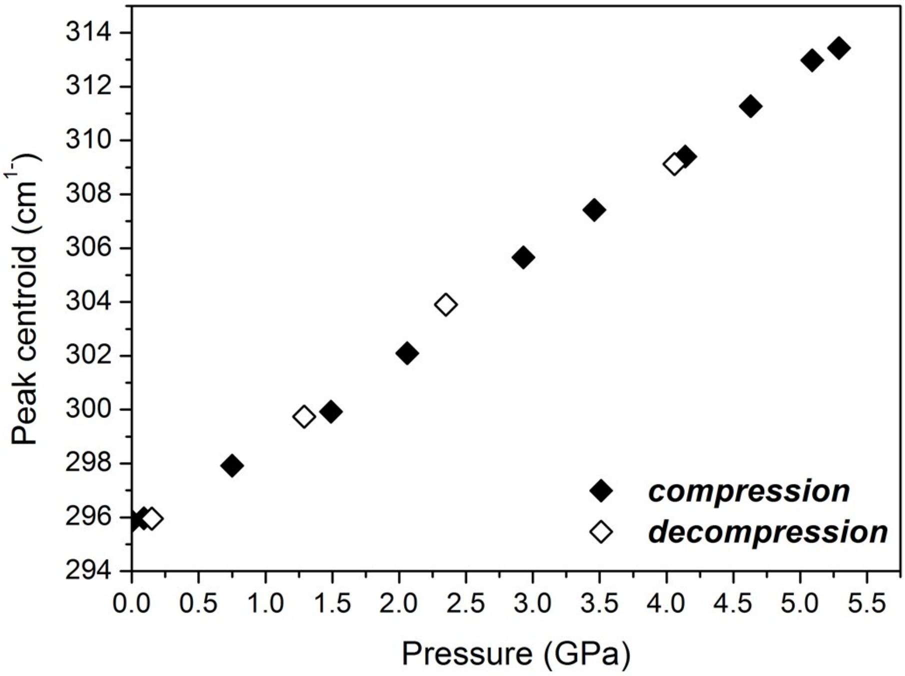

Figure S1. Comparison of energy of the phonon band for $SrF_2:Yb^{3+}$, Er^{3+} NPs at high pressure.

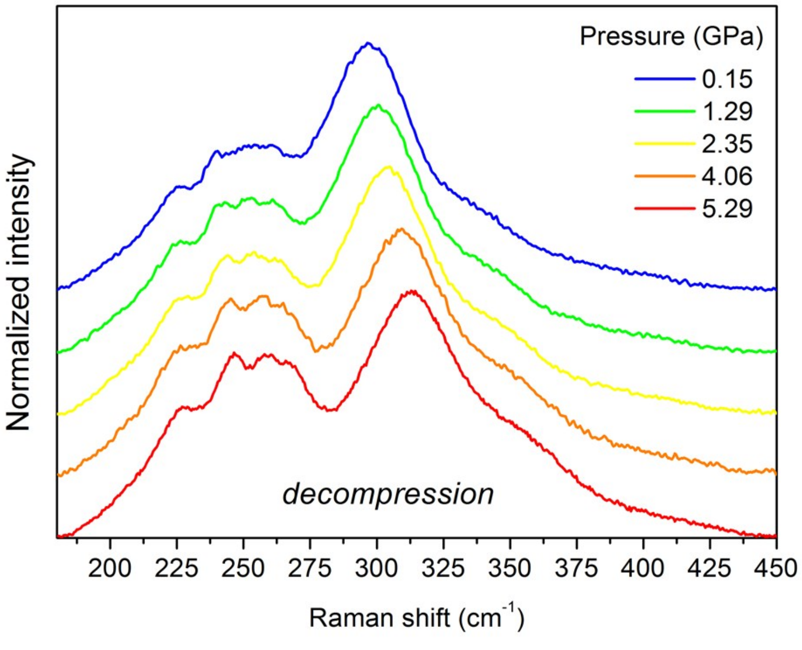

Figure S2. Raman spectra of $SrF_2:Yb^{3+}$, Er^{3+} sample at decreasing pressure (decompression).

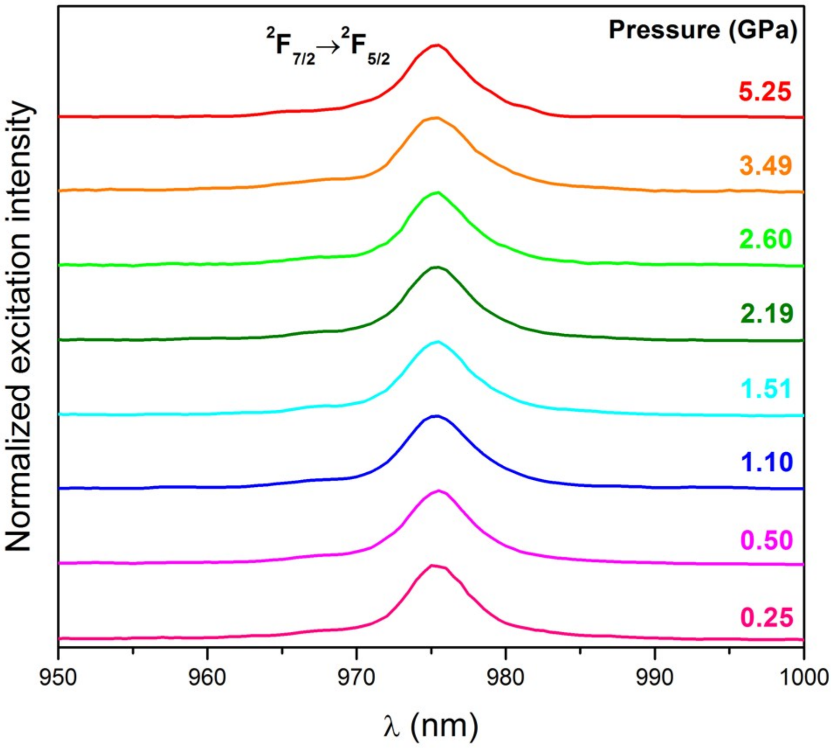

Figure S3. Excitation spectra of $SrF_2:Yb^{3+}$, Er^{3+} sample at increasing pressure; λ_{em}= 538 nm.

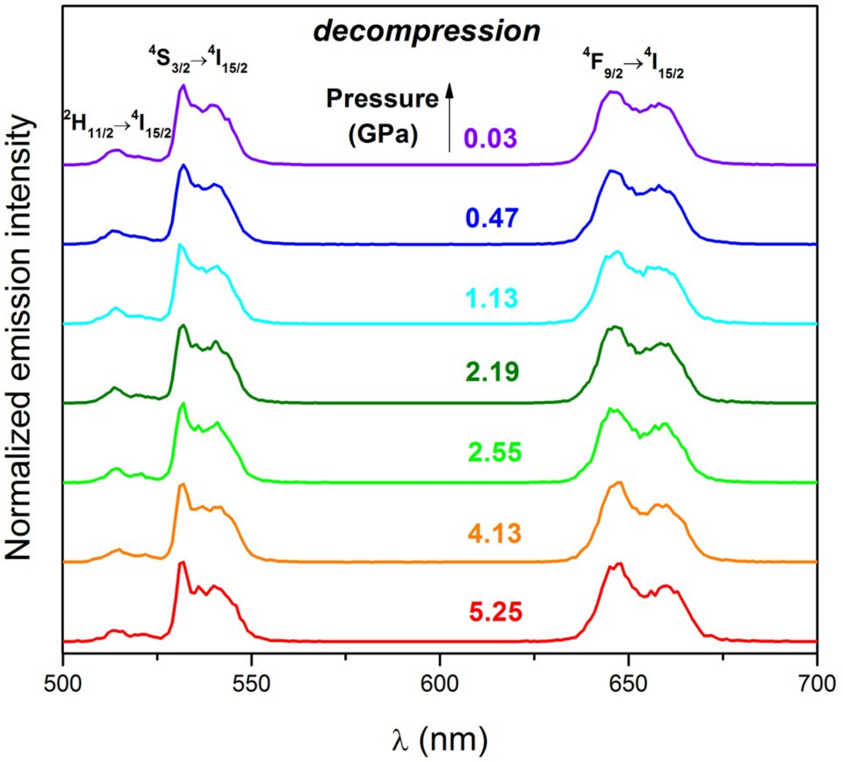

Figure S4. Emission spectra of $SrF_2:Yb^{3+}$, Er^{3+} sample at decreasing pressure (decompression); λ_{ex}= 980 nm.

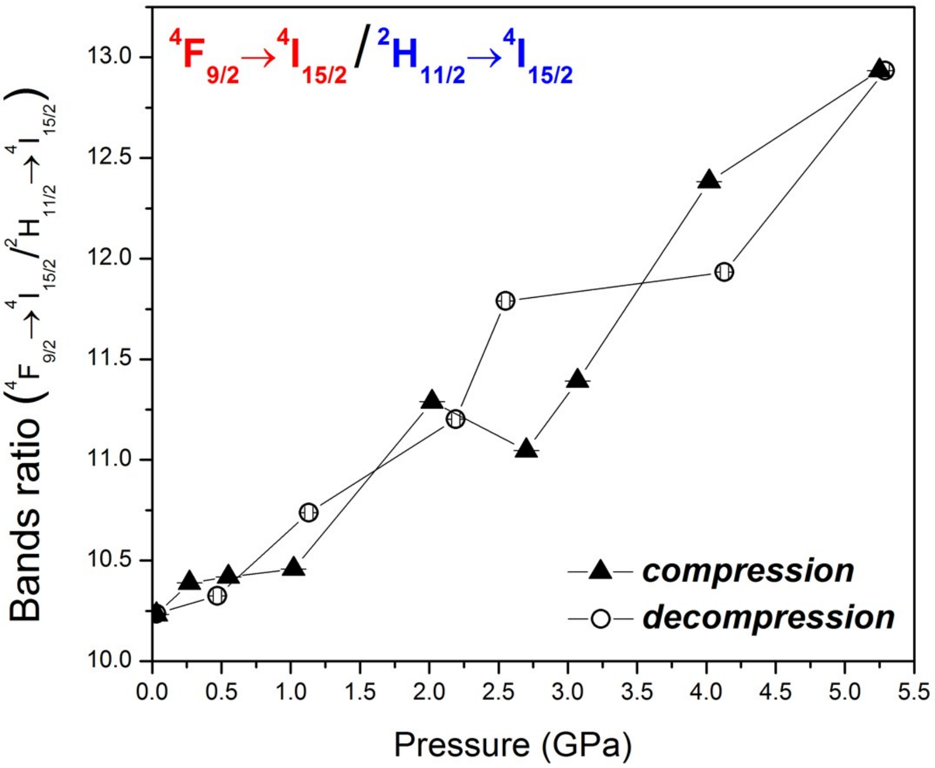

Figure S5. Comparison of $^4F_{9/2}\rightarrow ^4I_{15/2}/^2H_{11/2}\rightarrow ^4I_{15/2}$ bands ratio for SrF_2:Yb^{3+}, Er^{3+} sample at increasing and decreasing pressure; λ_{ex}= 980 nm.

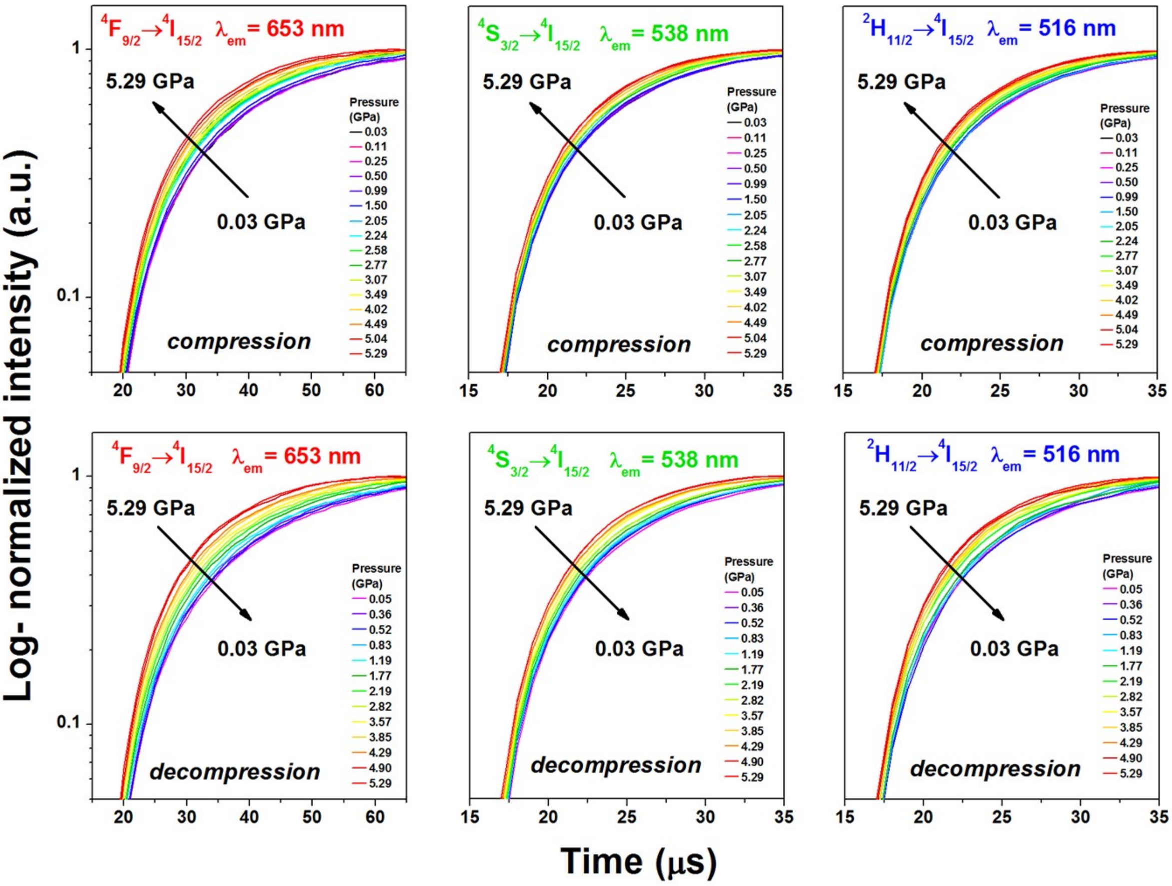

Figure S6. Magnified luminescence rise curves for $SrF_2:Yb^{3+}$, Er^{3+} sample at increasing (top) and decreasing pressure - decompression (bottom); λ_{ex}= 980 nm, λ_{em}= 653, 538 and 516 nm for: $^4F_{9/2} \rightarrow {}^4I_{15/2}$, $^4S_{3/2} \rightarrow {}^4I_{15/2}$ and $^2H_{11/2} \rightarrow {}^4I_{15/2}$ transitions, respectively.

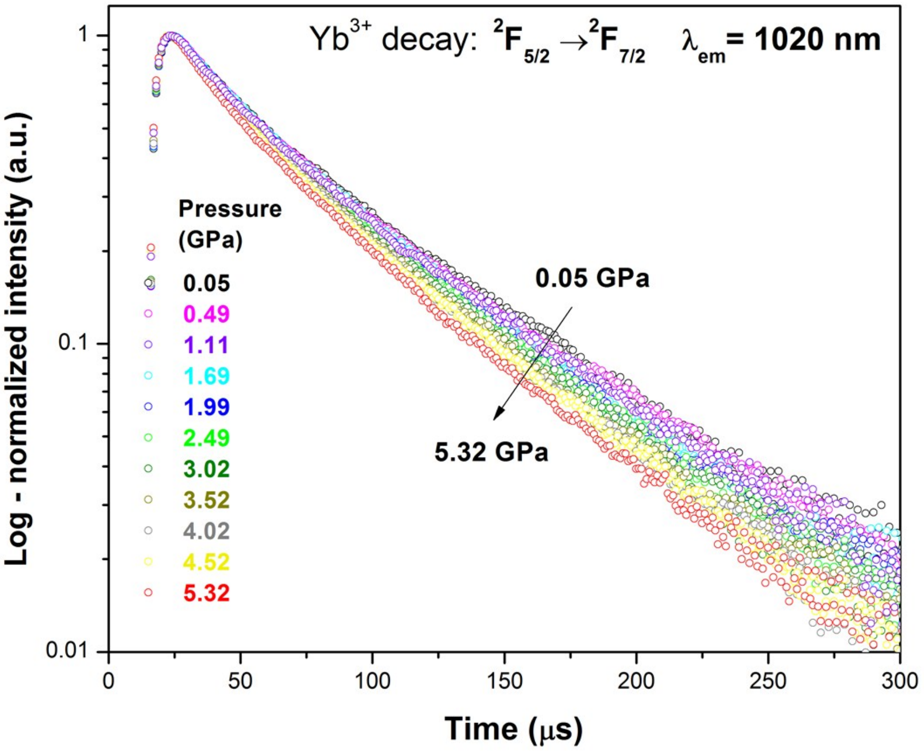

Figure S7. Yb^{3+} luminescence decay curves for $SrF_2:Yb^{3+}$, Er^{3+} sample at increasing pressure; λ_{ex}= 980 nm, λ_{em}= 1020 nm.

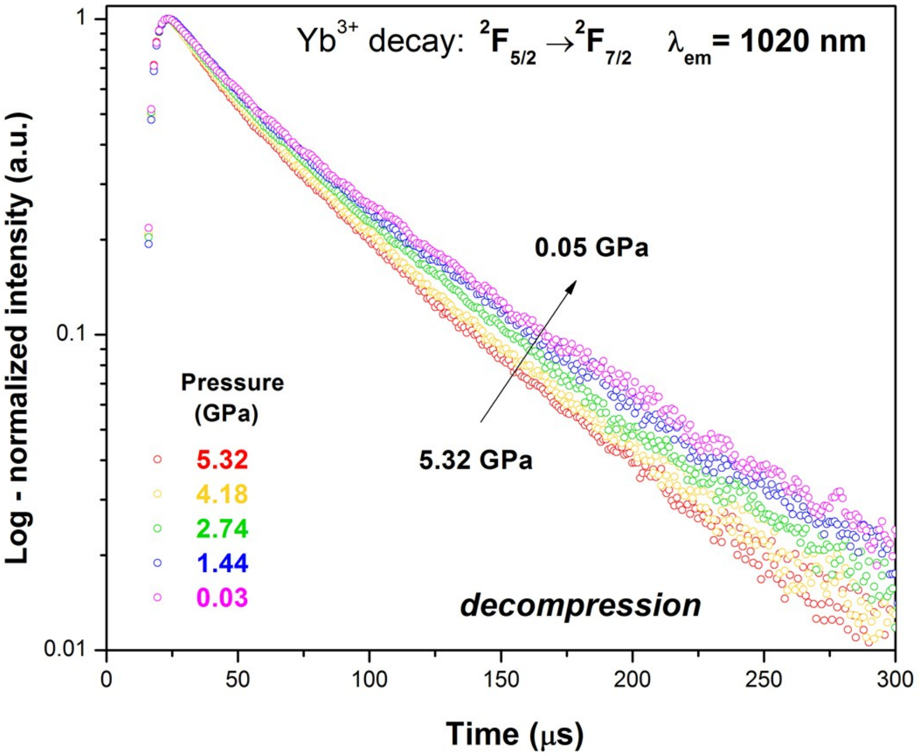

Figure S8. Yb^{3+} luminescence decay curves for $SrF_2:Yb^{3+}$, Er^{3+} sample at decreasing pressure (decompression); λ_{ex}= 980 nm, λ_{em}= 1020 nm.

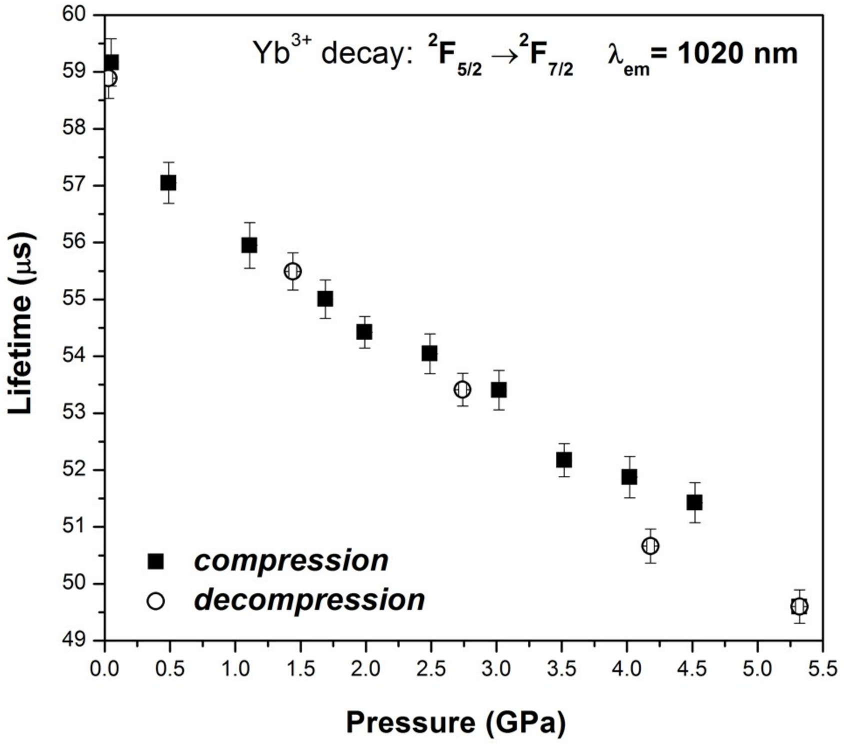

Figure S9. Luminescence lifetimes of Yb^{3+} ions, for $SrF_2:Yb^{3+}$, Er^{3+} sample at increasing and decreasing pressure; λ_{ex}= 980 nm, λ_{em}= 1020 nm.

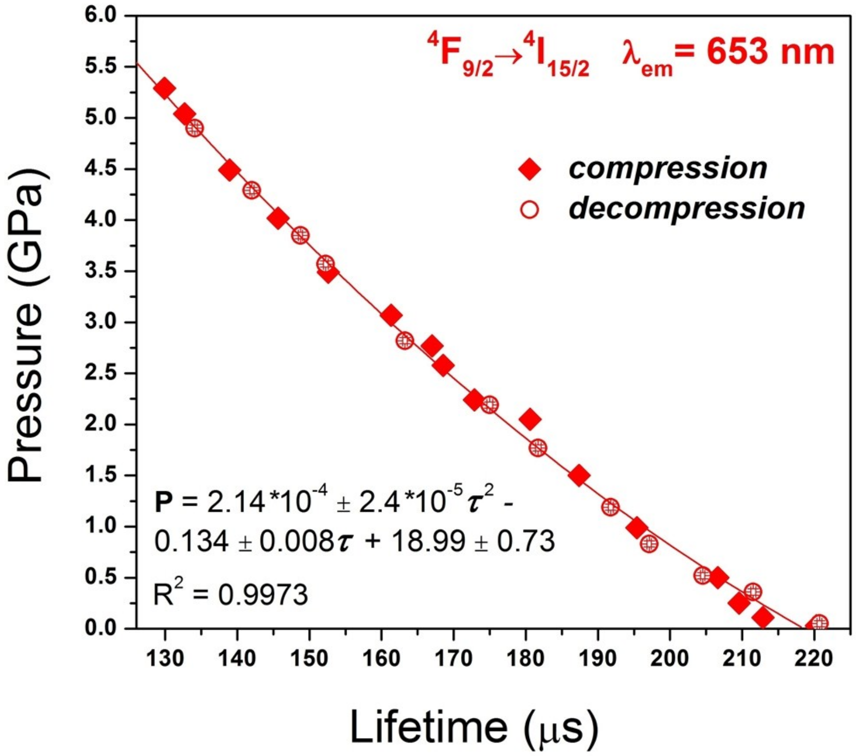

Figure S10. Determined pressure calibration curve based on $SrF_2:Yb^{3+}$, Er^{3+} lifetime; λ_{ex}= 980 nm, λ_{em}= 653 nm ($^4F_{9/2} \rightarrow {}^4I_{15/2}$ transition).

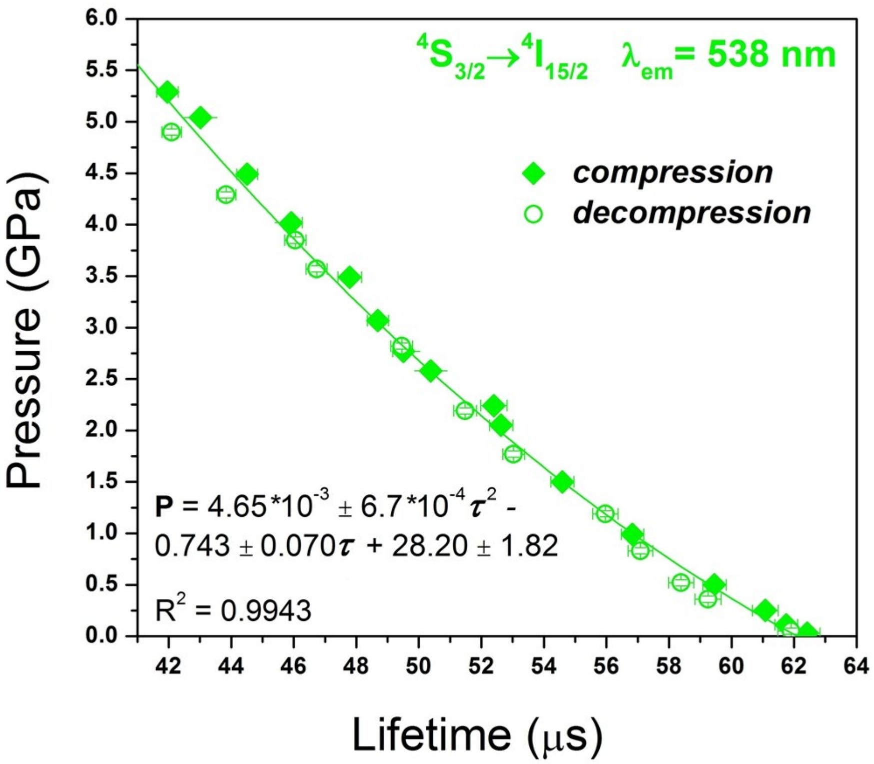

Figure S11. Determined pressure calibration curve based on $SrF_2:Yb^{3+}$, Er^{3+} lifetime; λ_{ex}= 980 nm, λ_{em}= 538 nm ($^4S_{3/2} \rightarrow {}^4I_{15/2}$ transition).

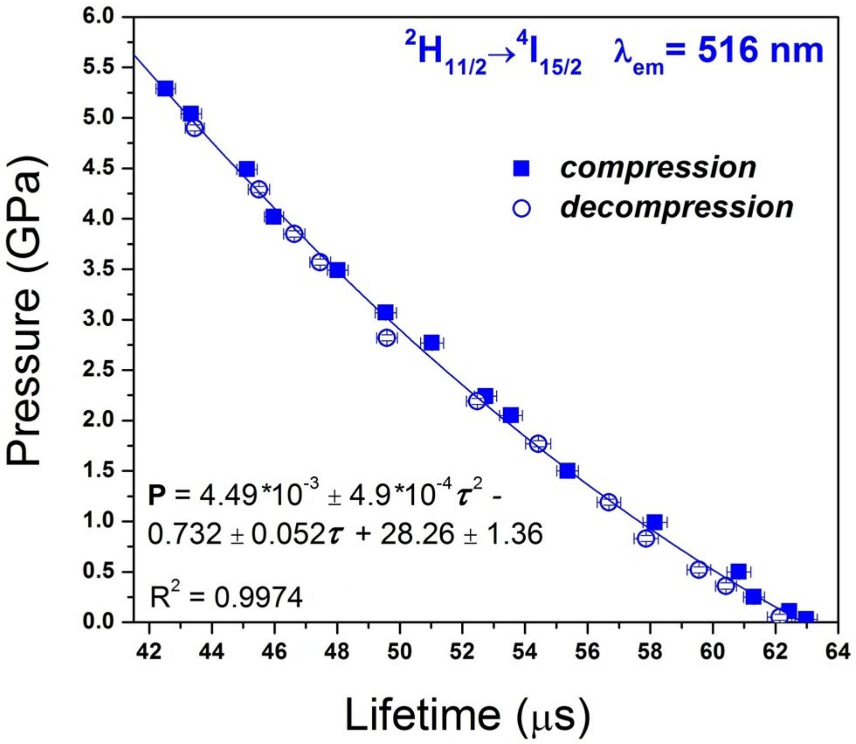

Figure S12. Determined pressure calibration curve based on $SrF_2:Yb^{3+}$, Er^{3+} lifetime; λ_{ex}= 980 nm, λ_{em}= 516 nm ($^2H_{11/2} \rightarrow {}^4I_{15/2}$ transition).

Pressure-induced changes in energy transfer rates

The balance of ETU excitation is given by competition of three kinds of processes: direct transfer (Yb-to-Er), back-transfer (Er-to-Yb) and cross-relaxation. The processes sum up and result in effective (total) energy transfer from Yb^{3+} to Er^{3+}, which results in Er^{3+} emission under Yb^{3+} excitation. External pressure results in an increase of all of the elementary processes, but also in increase of their effective sum.

The ET rates depend of the distance R between the two ions which participate in an elementary ET, the distance r between the dopant ions and their first coordination sphere ions and the shielding factors, $(1\text{-}\sigma)$. Noteworthy, Judd-Ofelt intensity parameters Ω_λ are present in the energy transfer rate equations. However, Ω_λ influence electric dipole-dipole and, to a less extent, dipole-quadruple mechanisms of ET;[6] quadruple-quadruple mechanism, which is more significant,[7] is not affected by Ω_λ. Consequently, changes in Ω_λ were considered negligible.

The dependence of the ET rates on R is quite straightforward: the rate of a particular transition is proportional to either R^{-6} (dipole-dipole mechanism, dd), R^{-8} (dipole-quadruple mechanism, dq) or R^{-10} (quadruple-quadruple mechanism, qq). Shielding factors can be calculated as $(1\text{-}\sigma_k) = \rho\ (2\beta)^{k+1}$, where $\beta = (1+\rho)^{-1}$, ρ being the overlap integral between 4f orbitals of the Ln ions and valence shells of ligand ions. The overlap integral depends on the distance between the central ion and the ligand ion r; in particular, ρ can be calculated as $\rho = \exp(a + br + cr^2)$. As the values of the overlap integrals corresponding to Yb^{3+} and Er^{3+} are very close, an average of the two was used, which led to the same shielding factors of both Yb^{3+} and Er^{3+} ions.[39] Using the values that should change with the pressure, a ratio of energy transfer rates at different pressures (by each of the mechanisms) can be calculated. Multiplying the ratio by the experimental lifetime at 100kPa, τ_0, one obtains trends in lifetimes caused by the changes in the ET rates due to the external pressure. In general, lifetime is an inverse of the corresponding rate, $\tau = 1/W$; thus, for arbitrary two states, $\tau_1/\tau_2 = W_2/W_1$. The calculated lifetime τ_P^{mm} by mm mechanism (mm stands for dd, dq or qq; m is the respective power, namely 6, 8 or 10) at a particular pressure P is given by:

$$\tau_P^{mm} = \tau_0 \frac{W_0^{mm}}{W_P^{mm}} = \tau^0 \frac{(1-\sigma_k)_0^2 (1-\sigma_{k'})_0^2}{(1-\sigma_k)_P^2 (1-\sigma_{k'})_P^2} \left(\frac{R_P}{R_0}\right)^m \qquad \text{(S1)}$$

Here, k and k' can be either 1 or 2, depending on *mm*; X_0 values (taken from experimental data) correspond to normal pressure, 100kPa; X_P values refer to pressure P; please note that $R_P/R_0 = r_P/r_0$. The distance ratios were obtained from the XRD data.

The resulting curves are shown in Fig. S11-S13 and illustrate how the lifetimes would change under pressure, given that ET occurs via single mechanism, either dd, dq or qq. It should not be interpreted as domination of any of the mechanisms. Basically, the curves show that both trend curvature and order of magnitude of lifetime changes can be reproduced via changes in ET rates, in particular in Ln-Ln distance and overlap integrals.

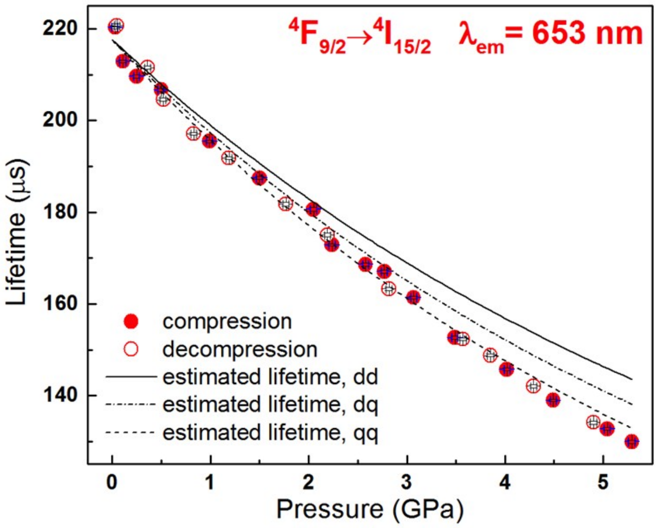

Figure S13. Experimental lifetimes of $^4F_{9/2} \rightarrow ^4I_{15/2}$ transition under compression and decompression (scatter) and theoretically estimated dependencies by dd, dq and qq mechanisms.

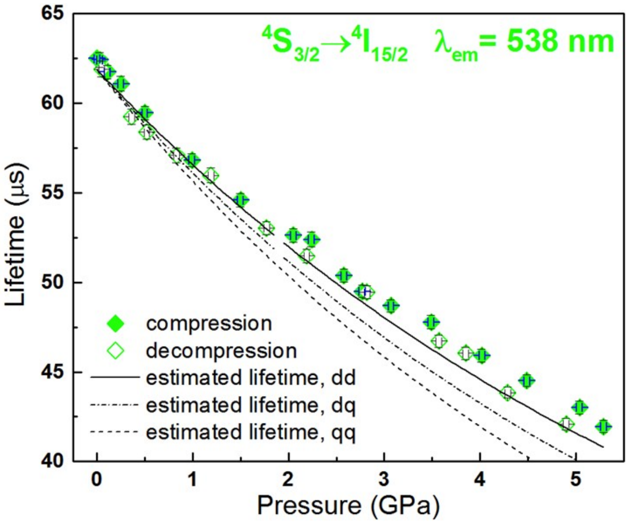

Figure S14. Experimental lifetimes of $^4S_{3/2} \rightarrow ^4I_{15/2}$ transition under compression and decompression (scatter) and theoretically estimated dependencies by dd, dq and qq mechanisms.

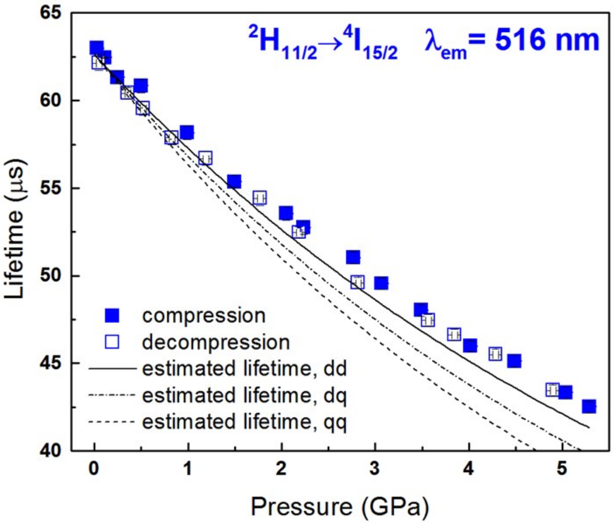

Figure S15. Experimental lifetimes of $^2H_{11/2} \rightarrow ^4I_{15/2}$ transition under compression and decompression (scatter) and theoretically estimated dependencies by dd, dq and qq mechanisms.

Theoretical analysis of non-radiative decay rates

We have assumed that number of phonons, *n*, in an elementary quenching act does not change with pressure; *n* was obtained as round of $\Delta E/\upsilon$, where ΔE is energy gap between the level being quenched and a level below it (measured between lower side of upper manifold emission peak and upper side of lower manifold emission peak, see Figure 10) and υ is phonon energy. The *n*, υ and Sr-F distance *r* were used to calculate multi-phonon relaxation rates, using the theory described by Pukhov,[8] with parameters from the paper by Orlovskii et al.[9] Single-phonon approximation applied: energy gap was considered to be bridged by *n* phonons of υ energy. The theory includes effects of temperature, phonon energy, coordination geometry and crystal field effects; noteworthy, energy gap law can be derived as special case from the theory. The obtained multi-phonon rates changed only slightly with pressure. If the multi-phonon processes were dominating in the observed kinetics, the lifetimes of $^4F_{9/2}$, $^4S_{3/2}$ and $^2H_{11/2}$ levels would have decreased by about 8%, 8% and 23%, respectively; noteworthy, the calculated multi-phonon decay lifetimes of $^2H_{11/2} \rightarrow ^4S_{3/2}$ transition are about 10 and 220 ns for 1- or 2-phonon process, respectively. Consequently, pressure-induced changes in phonon energy in SrF_2:Yb^{3+}, Er^{3+} are apparently less significant, comparing to that of ET rates.

The average rate of non-radiative phonon relaxation (by n phonons) of a transition between A and A' manifolds of a Ln^{3+} ion in solid (within the effective phonon model, with a single phonon frequency) is given by:

$$W_{A\to A'} = \frac{2^n}{c\nu}\eta^n \left(\frac{1}{\exp\left(\frac{hc\nu}{k_B T}\right)-1}+1\right)^n \sum_{k=2,4,6} \omega_{kn}^2 \left\langle A'J'||U^{(k)}||AJ\right\rangle^2 \tag{S2}$$

$$\omega_{kn}^2 = \frac{Z(2l+1)^2}{4h^2(2J+1)} \begin{bmatrix} l & l & k \\ 0 & 0 & 0 \end{bmatrix}^2 (2k+1)\left(C_{kn}(a_k^0)^2+\Phi_{kn}\right) \tag{S3}$$

Here, η is a parameter related to "infinitesimal" displacement "caused by phonon" and used to calculate the 4f-4f transition coupling to a phonon via crystal field; J and J' are total angular momenta, while A and A' represent other quantum numbers required to define the participating states; c is speed of light; υ is phonon frequency in reciprocal cm; n is number of phonons of υ frequency participating the decay; h is Planck constant; k_B is Boltzmann constant; T is absolute temperature; z is the number of ligand ions; quantum number l is 3 for 4f electrons; the symbol in Dirac bra-ket represents the doubly-reduced matrix elements of $\mathbf{U}^{(k)}$ irreducible unit tensor operator, used to characterize the intensities of the 4f-4f transitions; the expression in the first brackets in Eq. (1) is the temperature factor, which describes the dependence of the non-radiative decay rate on temperature. Other parameters are given by:

$$C_{kp} = \frac{(2p+2k)!}{(2k)!p!2^p} \tag{S3}$$

$$a_k^0 = \frac{4\pi e e_s \bar{\xi}^k}{(2k+1)r^{k+1}} \tag{S4}$$

The a_k^0 parameter represents the point charge crystal field model, or Coulomb part of the interaction between 4f electrons and ligand ions. Here, e is elementary charge; e_s is the effective charge of the s ligand (we have assumed that $e_s = -1$, i.e. formal charge of the fluorine anion); $\bar{\xi}$ is radius of optical electron, an intrinsic parameter of Ln^{3+} ion; r is the distance between the Ln ion and ligand ion.

$$\Phi_{kn} = \sum_i (b^0_{ki})^2 \tau_i^{2n} \sum_j^{int(p/2)} \frac{2n-4j+1}{(2j)!!(2n-2j+1)!!} T^2_{n-2j}(\tau_i) \qquad \text{(S5)}$$

$$T_{n-2j}(x) = \sum_{m=0}^{n-2j} \frac{(n-2j+m)!}{m!(n-2j-m)!(2x)^m} \qquad \text{(S6)}$$

$$b^0_k = \sum_i b^0_{ki} = 8\pi e^2 (G_s S_s^2 + G_\sigma S_\sigma^2 + \gamma_k G_\pi S_\pi^2)/7r \qquad \text{(S7)}$$

where $i = s, \sigma, \pi$. The b^0_k parameter represent the non-Coulomb part of the interaction, via the exchange charge mechanism. S_i are overlap integrals between the 4f electrons and s, σ, π orbitals of the ligand ion; $S_i = S^0_i \, exp(-\alpha_i R)$; $\gamma_k = 2 - k(k+1)/12$; G_s, G_σ, and G_π are the dimensionless parameters of the crystal field in the exchange charge model. In this paper, we have assumed that $G_s = G_\sigma = G_\pi = G$, and the values of ξ, G, S^0_i and α_i were obtained from the paper by Orlovskii et al.[9]

Phonon energy υ affects $W_{A \to A'}$ directly, and also affects the temperature factor. The parameter contains a $r^{-(k+1)}$ dependence of r. The Φ_{kn} function in Eq. (S2, S5) represents a part of non-radiative relaxation rate via exchange charges mechanism. The function depends on b^0_k parameters, which depend on overlap integrals between the 4f electrons of central ion and valence shells of ligand ions; it also depends on $1/r$. The η parameter mentioned above contains another dependence on r: $\eta = \langle u^2 \rangle / 6r^2$, u being the mentioned above infinitesimal displacement; η can be estimated as $\eta = \hbar/(8M\pi c \upsilon r^2)$, where M is reduced mass of the cation and anion of the host material, namely $M_{cat.}M_{an.}/(M_{cat.} + M_{an.})$.

References

1. Merrill, L.; Bassett, W. A. *Rev. Sci. Instrum.*, **1974**, *45*, 290-294.
2. Katrusiak, A. *Acta Crystallogr. Sect. A Found. Crystallogr.*, **2007**, *64*, 135–148.
3. Piermarini, G. J.; Block, S.; Barnett J. D.; Forman, R. A. *J. Appl. Phys.*, **1975**, *46*, 2774–2780.
4. Mao, H. K.; Xu, J.; Bell, P. M. *J. Geophys. Res.* **1986**, *91* (B5), 4673–4676.
5. Xcalibur CCD System, CrysAlisPro Software System, **2014**.
6. Malta, O. L, *J. Non. Cryst. Solids* **2008**, *354* (42–44), 4770–4776.

7. Shyichuk, A.; Câmara, S. S.; Weber, I. T.; Carneiro Neto, A. N.; Nunes, L. A. O.; Lis, S.; Longo, R. L.; Malta, O. L, *J. Lumin.* **2016**, *170*, 560–570.

8. Pukhov, K. K, *Phys. Solid State* **2008**, *50* (9), 1597–1604.

9. Orlovskii, Y. V.; Reeves, R. J.; Powell, R. C.; Basiev, T. T.; Pukhov, K. K, *Phys. Rev. B* **1994**, *49* (6), 3821–3830.